Graphene Transistors for Ambipolar Mixing at Microwave Frequencies

H. Madan[a], M. J. Hollander[a], J. A. Robinson[b] and S. Datta[a]

[a] Department of Electrical Engineering, The Pennsylvania State University, University Park, PA 16802, USA
[b] Department of Materials Science and Engineering, The Pennsylvania State University, University Park, PA 16802, USA

This work presents a detailed study of the graphene RF mixer in the ambipolar configuration, using quasi-free-standing epitaxial graphene on SiC. Record high conversion gain is achieved through use of optimized growth and synthesis techniques, metal contact formation, and dielectric materials integration. Hydrogen intercalation is utilized to isolate the graphene from the underlying SiC substrate and improve transport properties. Low contact resistances at the metal-graphene interface are realized using an oxygen plasma pre-treatment, while dielectric seeding is achieved using a direct deposited layer of HfO_2 before ALD film growth. Output characteristics of the graphene transistor are analyzed and the effects on mixer performance are explained. A graphene RF transistor is designed with gate length 750nm, width 20μm, and equivalent oxide thickness ~2.5nm in order to achieve record high conversion gain of -14 and -16dB at LO power 0dBm at 4.2 and 10GHz, respectively, 100× higher than previously reported ambipolar mixing.

Introduction

In recent years, graphene has gained interest for use in RF electronic devices due to its high carrier mobility, symmetric electron and hole conduction, and ambipolar behavior. These properties have allowed for novel RF applications, including a single transistor triple-mode amplifier (1) and a single transistor ambipolar mixer (2), which can provide unique advantages over conventional designs. For the single transistor mixer, graphene's ambipolar nature (Fig. 1a) allows for suppression of odd order harmonics at the Dirac point, where small signal output at the drain is given as:

$$i_{ds} = g_m v_{gs} + g'_m v_{gs}/2 + g''_m v_{gs}/6 + \ldots \quad [1]$$

Suppression of odd order harmonics leads to improved conversion gain over conventional single transistor implementations and is the result of both g_m and g''_m vanishing at the Dirac point, where g'_m displays a local maximum (Fig. 1b). More conventional mixer designs have also been implemented, showing resistive (3) and drain mixing (4).

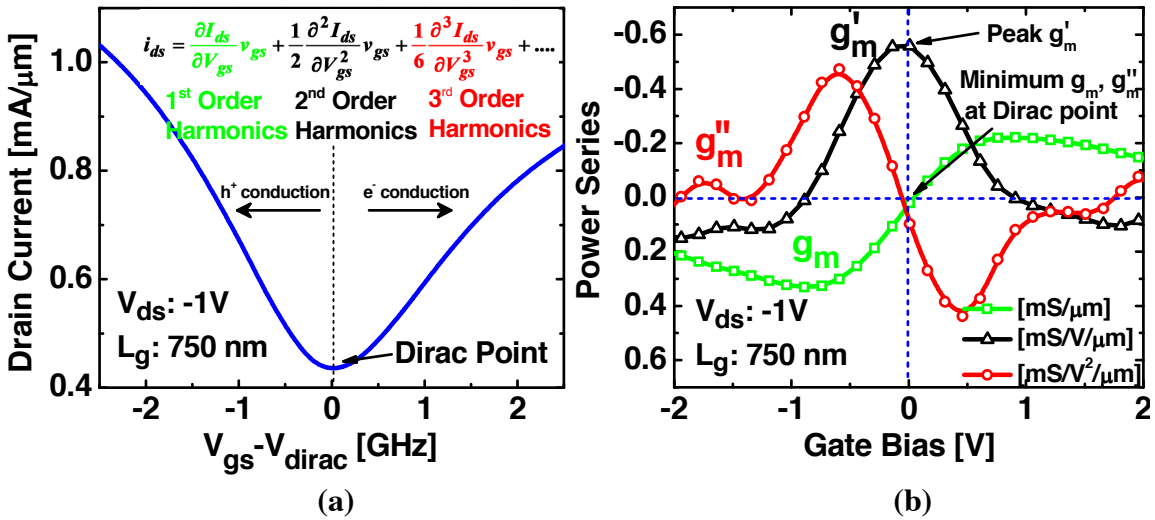

Figure 1. Ambipolar conduction leads to high conversion gain and suppression of odd order mixing products at transistor output. (a) Transfer curve of graphene FET showing ambipolar behavior. (b) Extracted first, second, and third order components of drain current showing peak g'_m as well as minimum g_m and g''_m at the Dirac point (5).

Although initial mixer demonstrations have been successful, ultimate performance has been limited by high contact resistance, low mobility, and low transconductance. In this work, these limitations are addressed for epitaxial graphene transistors patterned on a SiC substrate. Hydrogen intercalation is used to boost mobility by >2× relative to conventional epitaxial graphene on SiC, contact resistances of 100 ohm-μm are achieved using an oxygen plasma pre-treatment, and high transconductance is achieved using a highly scaled HfO_2 gate dielectric.

Synthesis, Materials, and Fabrication

Graphene is prepared on (0001) oriented, semi-insulating 6H-SiC through combination of sublimation and hydrogen intercalation leading to carrier mobilities as high as 3000 $cm^2/V \cdot sec$ at 10^{13} carriers per cm^{-2}. Sublimation of Si takes place from the Si-face at 1625°C in 1 Torr Ar, where high temperature growth conditions lead to significant step-bunching and a terraced morphology across the substrate. Following synthesis, epitaxial graphene is characterized via Raman spectroscopy, x-ray photoelectron spectroscopy (XPS), and Lehighton non-contact mobility and sheet resistance (LEI,Inc). Raman spectroscopy confirms the successful growth of monolayer epitaxial graphene across the (0001) SiC terrace and bilayer epitaxial graphene on the terrace step edge (6)-(8).

Hydrogen Intercalation

Hydrogen intercalation is a key step in maintaining high carrier mobility for epitaxial graphene, where hydrogen intercalated samples show an average increase in mobility of >2× despite a large increase in carrier concentration. In this step, samples are exposed to molecular hydrogen at 1050°C in 600 Torr Ar/H_2 after the Si sublimation step. Subsequent to hydrogen intercalation, peak fitting of the 2D Raman peak indicates

bilayer graphene across the terrace and multi-layer graphene at the step edge, which indicates the successful passivation of the carbon buffer layer through the formation of an additional layer of graphene. X-ray photoelectron spectroscopy (XPS) further confirms successful passivation, where the S1 and S2 components of the C1s spectra present in as-grown epitaxial graphene are eliminated upon full hydrogen intercalation (Fig. 2a).

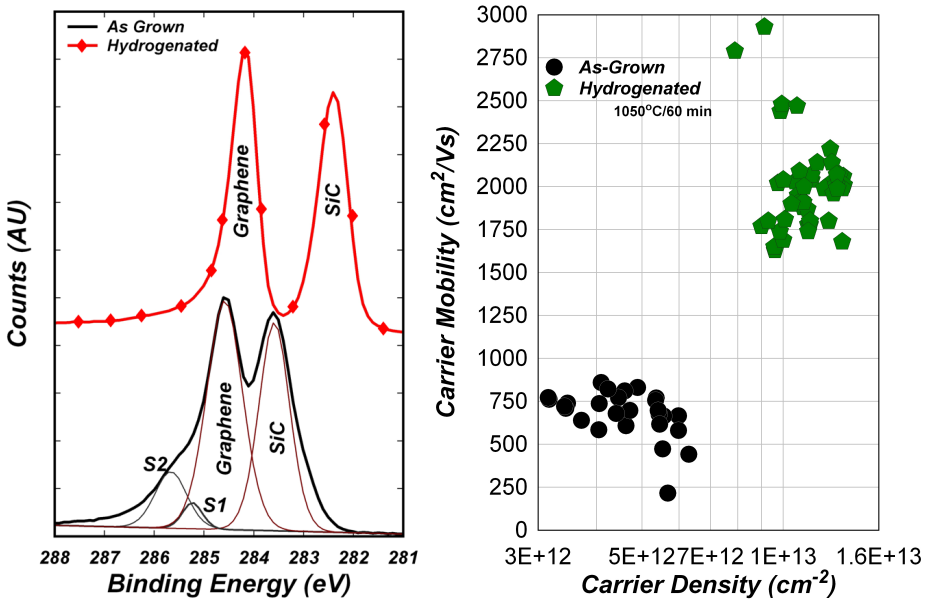

Figure 2. (a) X-ray photoelectron spectroscopy, and (b) Hall transport properties of as-grown and hydrogenated graphene (9).

Figure 2b summarizes the change in Hall mobility and carrier density with hydrogen intercalation, where improved transport properties are attributed primarily to a reduction in charged impurity scattering. Additional evidence has also been presented suggesting a reduction in remote surface optical phonon scattering for hydrogen intercalated samples (10), (11).

Low Resistance Metal Contacts

High contact resistances can severely limit ultimate device performance. In this work, an oxygen plasma pre-treatment is used to reduce the specific contact resistance (ρ_c) and improve contact resistance to values as low as 100 ohm-μm (Ti/Au). Specific contact resistance, a measure of the metal/graphene interfacial resistance, is highly sensitive to interfacial reactions or device processing conditions that could lead to interfacial contamination and is an ideal way to evaluate the quality of the metal/graphene electronic interface. We find that the utilization of an oxygen plasma-etch serves well to remove residual resist prior to metal deposition when implemented properly and can lead to a significant improvement in ρ_c. Specifically, utilization of a low power O_2 plasma treatment ("ash") prior to metal deposition provides superior contact resistances compared to un-treated or post-processed contacts (12). Although there is degradation in the structure of the graphene (evidenced by the increase in Raman D/G ratio) even under the most benign conditions, ρ_c is shown to improve with O_2 plasma treatment as the treatment time increases from 30 – 90 sec to an average value of 4 x 10^{-7}

Ohm-cm^2. Upon reaching 120 sec, ρ_c begins to degrade and is correlated with severe deterioration in the Raman 2D peak intensity, suggesting that the bulk of the sp^2-bonding expected in graphene has been destroyed. Following the low power O_2 plasma etch to remove photoresist residue, post-processing heat treatments of the contacts further improve contact resistance 5x to an average of 7 x 10^{-8} Ohm-cm^2.

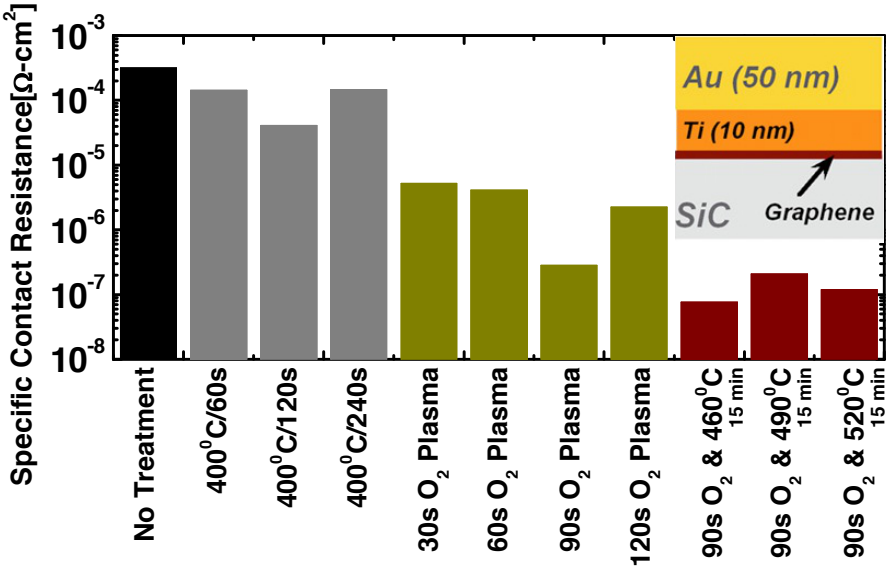

Figure 3. Specific contact resistance as a function of pre and post-treatment. Use of an oxygen plasma pre-treatment in combination with a post-metallization anneal in forming gas produces the lowest specific contact resistance (12).

Dielectric Integration

Gate dielectrics were deposited using an e-beam physical vapor deposition (EBPVD) seeded ALD process (2 nm HfO_2 seed / 10 nm ALD HfO_2) (13). Use of the two-step EBPVD seeded ALD process allows for scaling the EOT to ~2.5 nm while maintaining uniform coverage and without significantly degrading transport properties. This is accomplished primarily through dielectric screening of any additional charged impurity scattering centers introduced by the dielectric. Whereas previous work showed that use of an EBPVD seeded ALD process can lead to improved transport properties for epitaxial graphene samples (13), similar experiments on hydrogen intercalated graphene show little improvement in transport properties. Using temperature dependent measurements of Hall mobility in combination with models for the temperature and carrier dependent behavior of various scattering phenomenon in ideal graphene samples, it is shown that this difference in behavior between hydrogen intercalated graphene and non-hydrogen intercalated is due to the higher initial density of as-grown charged impurity scattering centers in non-hydrogen intercalated graphene (10). This initial high density of charged impurity scattering centers explains the low mobility for these samples and the reason why high-k dielectrics can produce such a large improvement in transport properties through dielectric screening.

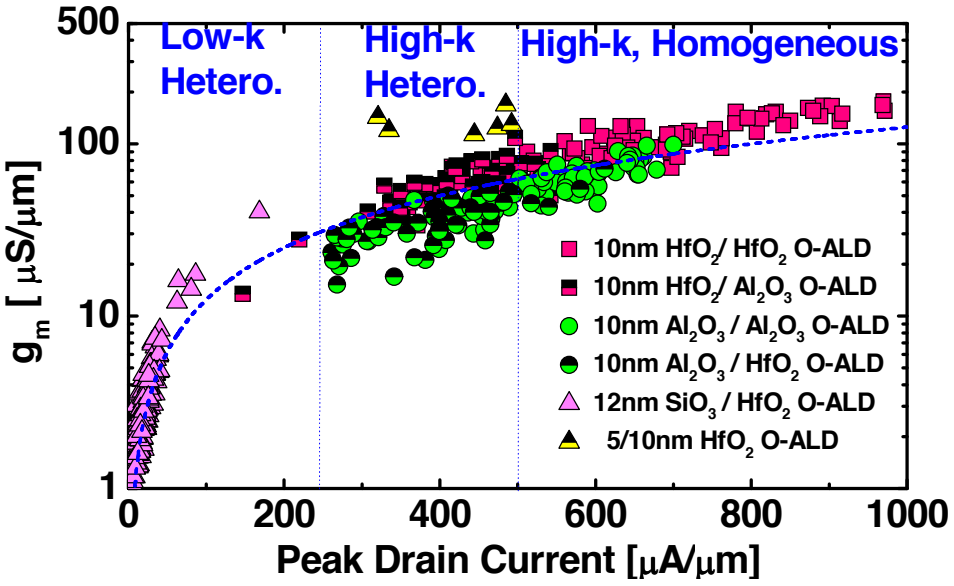

Figure 4. Scatter plot showing peak transconductance and peak drain current for several hundred graphene transistors with low and high-k dielectrics deposited using the two-step EBPVD seeded ALD growth technique. The HfO_2 / HfO_2 gate dielectric yields the highest performing devices (13).

For the case of hydrogen intercalated graphene, measurements before and after dielectric integration show similar mobilities, indicating that any benefit due to dielectric screening is offset by an increase in the density of charged impurity scattering centers with dielectric incorporation. Still, this gate dielectric represents an optimized path for limiting mobility degradation with dielectric integration, where use of low-k dielectrics offer little to no dielectric screening and still incorporate a significant number of additional charged impurity scattering centers. Figure 4 plots the peak transconductance and peak drain current for several hundred graphene transistors using low and high-k dielectrics deposited using the two-step EBPVD seeded ALD technique. From this plot, it is clearly seen that the high-k dielectrics lead to improved performance. Interestingly, it is also observed that homogeneous dielectrics (where EBPVD seed and ALD film are the same material) offer higher transconductance and drive currents as compared to heterogeneous dielectrics.

Besides improved transport relative to low-k dielectrics, the high-k two-step EBPVD seeded ALD process significantly improves uniformity and coverage of the ALD grown dielectric compared to non-seeded deposition techniques. Improved coverage leads to a smaller number of pinholes and significantly reduced surface roughness, which can negatively impact device performance or lead to dielectric breakdown. These improvements allow scaling of the gate dielectric to 10-12 nm and lead to the low EOT of ~2.5 nm.

Device Fabrication

Graphene transistors were patterned using standard photolithographic techniques (Fig. 5). Source/drain contacts were deposited using a metal-liftoff process (Ti/Au 10/100 nm). Gate dielectrics were blanket deposited over the sample using the EBPVD

seeded ALD process (10 nm HfO2) discussed previously, after which a RIE etch was used to remove the dielectric from the metal pads. A two finger, ground-signal-ground design was selected to facilitate RF characterization, with a gate length of 750 nm and a combined gate width of 20 μm.

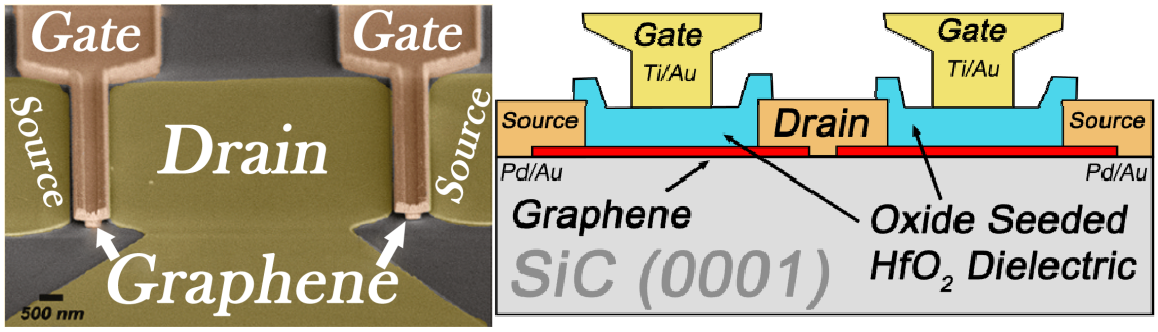

Figure 5. (a) False color SEM micrograph of two-finger graphene RF transistor with T-gates. (b) Schematic cross-section of graphene transistor with Lg=750nm and W=20µm. 10nm HfO2 gate oxide was grown by EBPVD seeded ALD as described previously (5).

Graphene FET Performance

Transfer curves (I_{ds}-V_{gs}) from V_{ds}=50mV to 1V were captured for the HfO_2 gated graphene transistors, exhibiting V_{Dirac} near V_{gs}=0V and near symmetric electron and hole branches (Fig. 6a). Family of curves (I_{ds}-V_{ds}) were measured from V_{gs}=0 to -3V showing weak saturation behavior typical of the semi-metal graphene (Fig. 6b). On-off ratios >2 and drive currents of 1.1 mA/µm at V_{ds}= -1V are attributed to the high mobility and low contact resistance in these samples. Peak transconductance is found to be 330 µS/µm (Fig. 7), which is attributed to the relatively small EOT for these devices (~2.5 nm) as well as the high mobility of the hydrogen passivated epitaxial graphene.

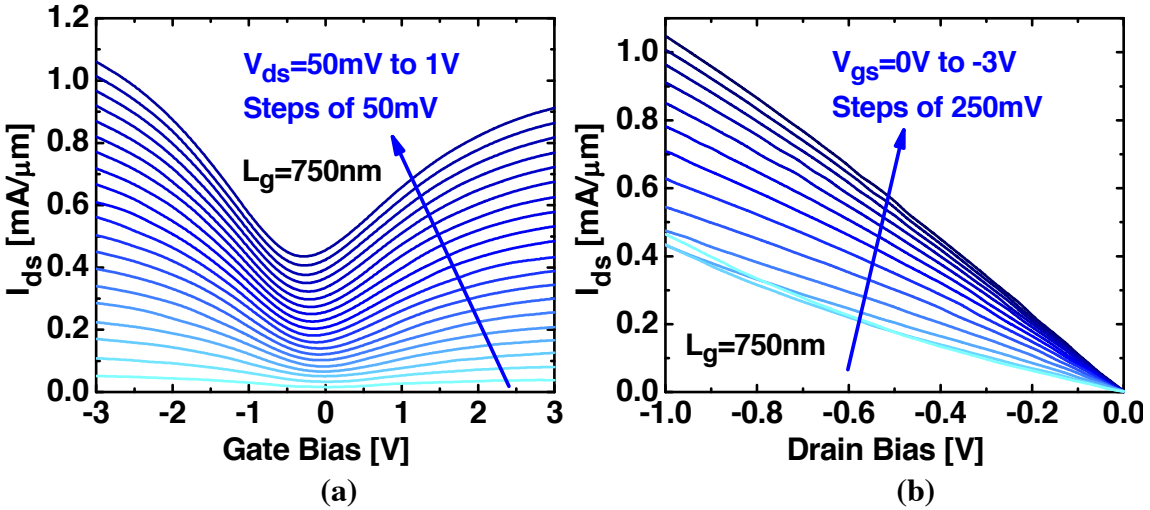

Figure 6. (a) Transfer curves (I_{ds}-V_{gs}) from V_{ds}=50mV to 1V exhibiting V_{Dirac} near V_{gs}=0V and near symmetric electron and hole branches. (b) Family of curves (I_{ds}-V_{ds}) from V_{gs}=0 to -3V showing weak saturation behavior (5).

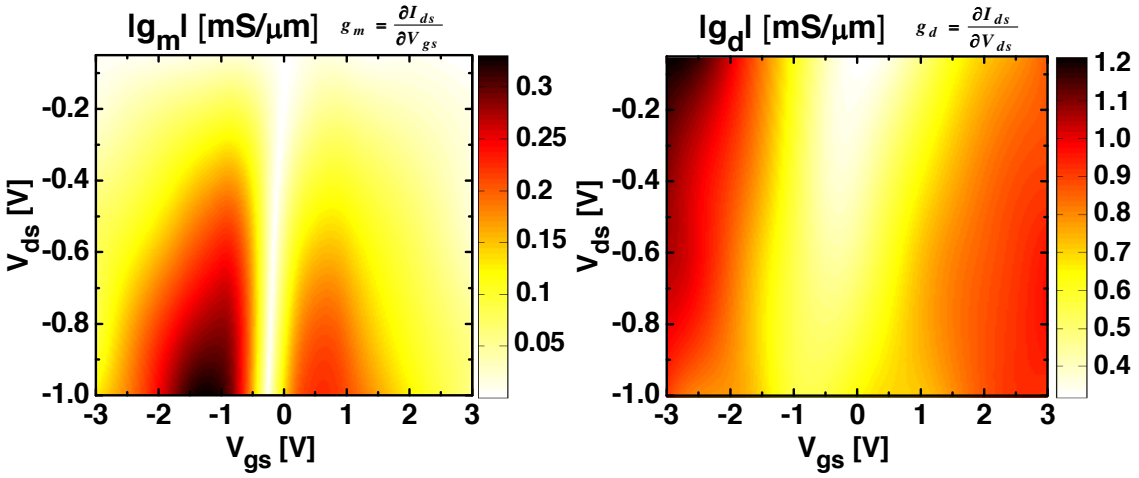

Figure 7. Color maps of absolute normalized transconductance (g_m) and output conductance (g_d) as a function of drain bias (V_{ds}) and gate bias (V_{gs}) indicating a peak transconductance of 330 μS/μm (5).

RF performance is excellent, exhibiting peak intrinsic current gain cutoff frequency (f_T) of 110 GHz at a gate length of 75 nm with V_{ds}= -1V, where intrinsic f_T was extracted from measured S-parameters using a standard short-open de-embed process to remove the effect of probe and pad parasitics. An intrinsic f_T of 15.3 GHz and intrinsic f_{Max} of 10.6 GHz are extracted from short circuit current gain and unilateral gain, respectively, for the 750 nm long device (Fig. 8a). Intrinsic f_T is found proportional to the inverse of L_g, although extrinsic performance is limited by parasitics at small gate lengths (Fig. 8b). Still, we report an excellent peak extrinsic $f_T \cdot L_g$ ~5 GHz·μm for an L_g of 750 nm (Fig. 8b). Effective injection velocity between 1.1 and 2.5x10^7 cm/sec is extracted from the small signal parameters for these devices.

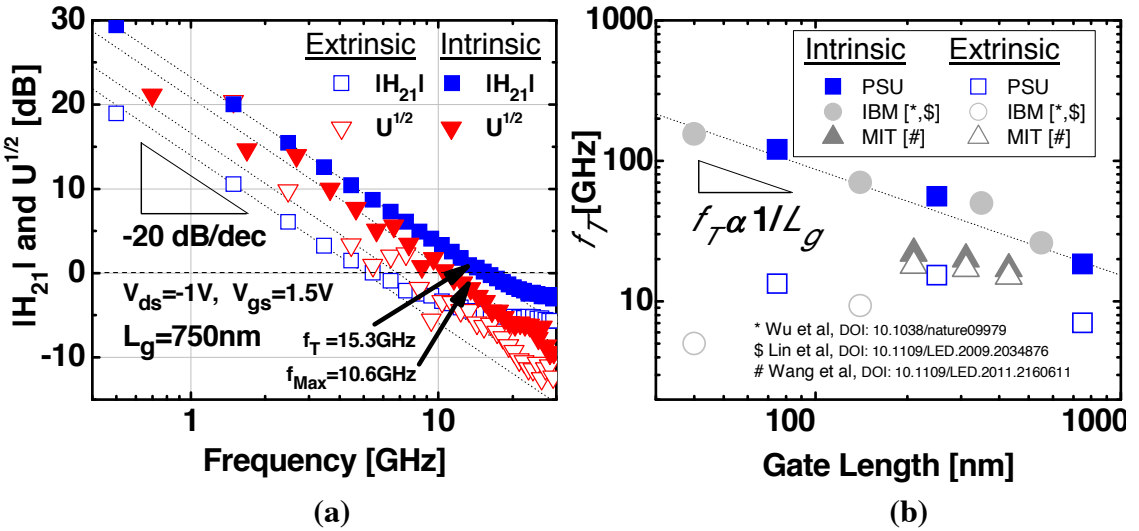

Figure 8. (a) Short circuit current gain and unilateral power gain of graphene transistor at V_{ds}=-1V and V_{gs}=1.5V. Intrinsic values are extracted using a short-open de-embed process in order to remove probe and pad parasitics. (b) Intrinsic and extrinsic f_T as a function of gate length, showing increasing effect of parasitics on extrinsic device performance as well as the expected dependency of f_T on L_g (5).

Mixer Performance

Ambipolar mixing is achieved through gate mixing of the LO and RF input signals (Fig. 9a). The LO and RF inputs of 4.2 (10) and 4 (9.8) GHz, respectively, were combined using an external power combiner. A plot of g_m' versus V_{gs} and V_{ds} identifies the Dirac point as the optimal bias point for maximum conversion gain (Fig. 9b) due to the fact that $P_{IF} \propto g_m'$. Fig. 9c shows the output spectrum at the Dirac point for LO power 0 dBm and RF power -15 dBm, displaying record conversion gain of -14 (-16) dB. Mixer performance was evaluated as a function of gate bias showing suppression of odd order harmonics at the Dirac point as well as confirming peak conversion gain at the Dirac

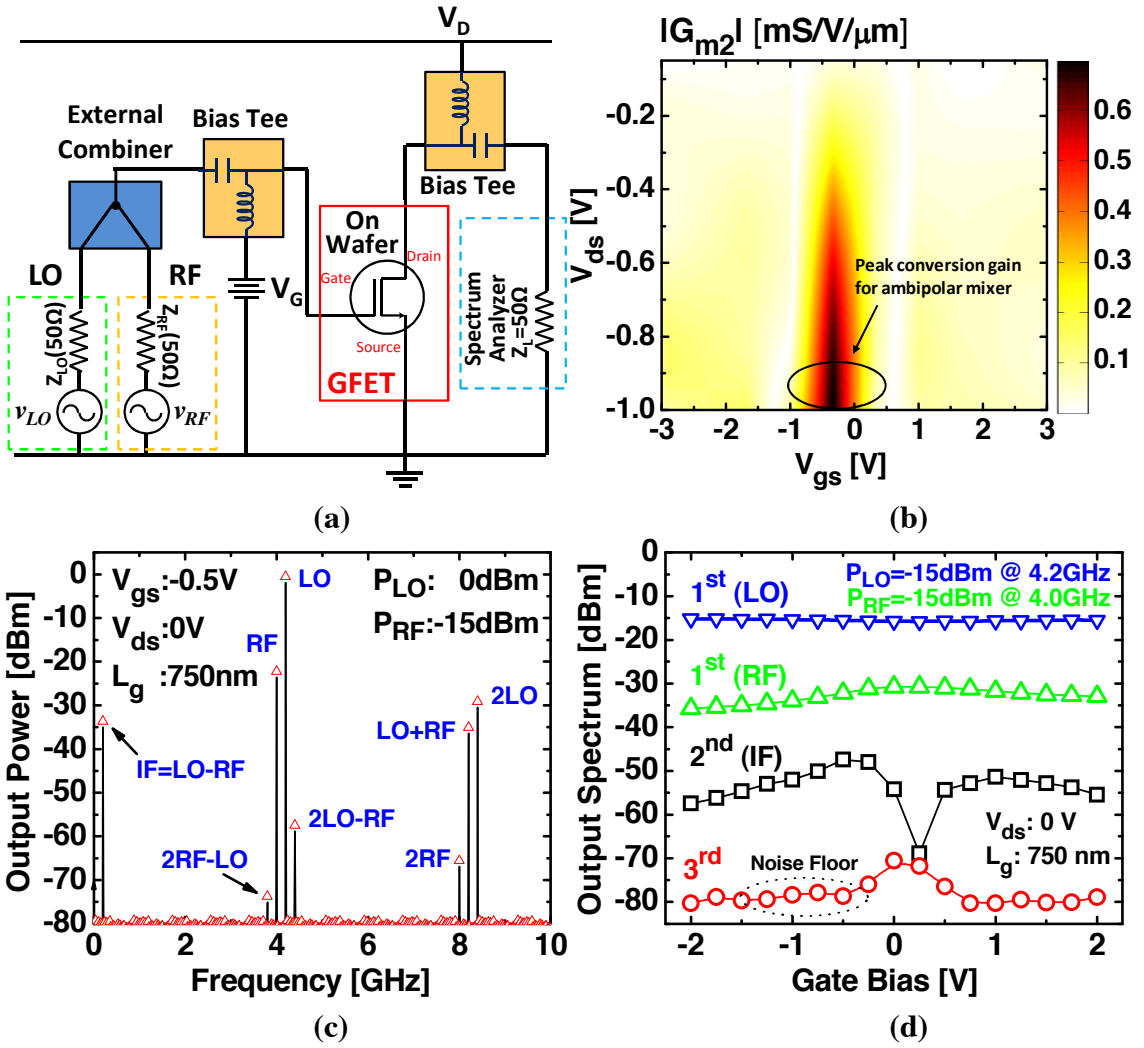

Figure 9. Peak conversion gain is achieved using ambipolar mixing at the gate terminal. (a) Measurement setup for ambipolar graphene mixer. (b) Measured g_m' ($P_{IF} \propto g_m'$) as function of V_{gs} and V_{ds} shows peak g_m' and indicates that maximum conversion gain should occur at the Dirac point. (c) Output spectrum for graphene ambipolar mixer, showing first, second, and third order mixing products as well as record high conversion gain of -14 dB at LO 0 dBm. (d) Measured output spectrum as a function of V_{gs} shows suppression of odd order harmonics and confirms peak conversion gain at the Dirac point (5).

point. High frequency and high gain mixer performance in this work is attributed to highly scaled EOT, high mobility, and low contact resistance

Benchmark

Conversion gain as a function of LO power shows linear performance up to 0 dBm for ambipolar mixing (Fig. 10). Conversion gain versus LO power shows higher conversion gain for ambipolar gate mixing as compared to resistive drain mixing. This work represents the highest performance graphene based mixer yet reported and, furthermore, utilizes the smallest physical width (20µm) of all reported graphene mixers, where increased width is expected to show increased conversion gain. High frequency and high gain mixer performance in this work is attributed to highly scaled EOT, high mobility, and low contact resistance compared to other graphene based mixers (Table I).

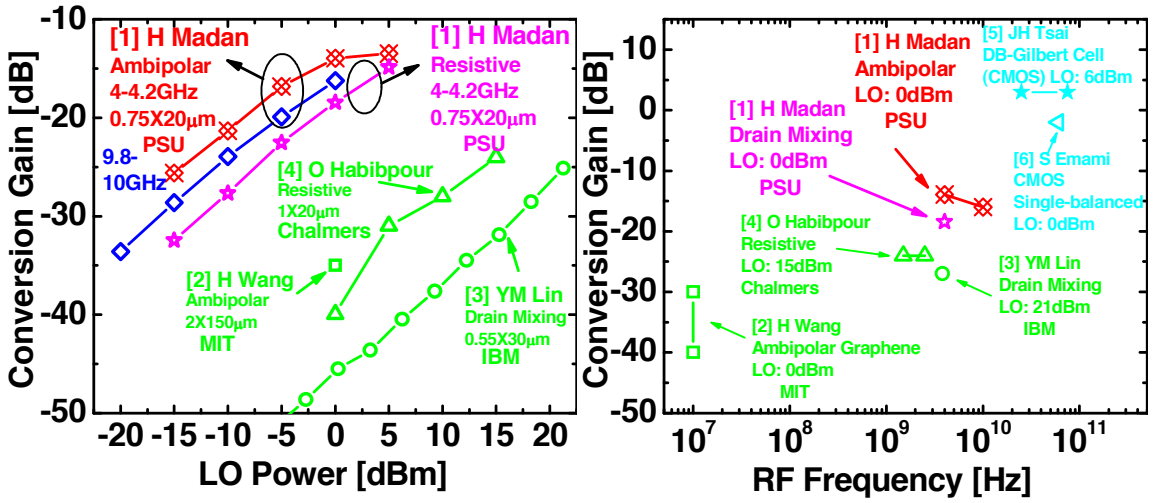

Figure 10. Record high conversion gain of -14dB for graphene based device at 4GHz demonstrated using ambipolar gate mixing and gate width of only 20µm. (a) Conversion gain versus LO power. (b) Conversion gain versus frequency showing operation up to 10GHz (5).

TABLE I. Conversion Gain Benchmark Parameters

Reference	# of FETs	L_g [µm]	W [µm]	t_{ox}[nm] (seed/oxide)	$g_{m,pk}$ [µS/µm]	V_{gs} [V]	V_{ds} [V]	R_{con} [Ω·µm]
[1] H Madan et al,(Amb.) IEDM 2012	1	0.75	20	2/10 (HfO_2)	330	0	-1	100
[1] H Madan et al,(Resis.) IEDM 2012	1	0.75	20	2/10 (HfO_2)	330	-0.5	0	100
[2] Wang et al, DOI: 10.1109/LED.2010.2052017	1	2.0	150	5/25 (SiO_2/Al_2O_3)	5.5	-0.2	--	2-5k
[3] Lin et al, DOI: 10.1126/science.1204428	1	0.55	30	2/20 (Al_2O_3)	80	-3	2	600
[4] Habibpour et al, DOI: 10.1109/LED.2011.2170655	1	1	20	2/25 (Al_2O_3)	35 [0.1V]	1	0	560
[5] Tsai et al, DOI: 10.1109/LMWC.2007.892934	10	--	--	--	--	--	--	--
[6] Emami et al, DOI: 10.1109/RFIC.2005.1489619	2	0.13	80	--	--	--	--	--

Conclusions

In conclusion, hydrogen intercalated graphene transistors with optimized contacts and gate dielectric were used to demonstrate record high conversion gain for a single graphene transistor ambipolar mixer. Ambipolar gate mixing was shown to suppress odd order harmonics and was found to outperform resistive drain mixing. Increased performance is anticipated by reducing D_{it} and further scaling EOT, which may enable graphene based ambipolar mixers to soon become competitive with conventional Gilbert cell mixers.

Acknowledgments

This research was sponsored by Office of Naval Research. (Grant # N00014-12-C-0124, monitored by Dr. Peter Crag)

References

1. X. Yang, G. Liu, A. A. Balandin and K. Mohanram, *ACS Nano,* **4**, 5532 (2010).
2. H. Wang, A. Hsu, J. Wu, J. Kong and T. Palacios, *IEEE Electron Device Letters,* **31**, 906 (2010).
3. O. Habibpour, S. Cherednichenko, J. Vukusic, K. Yhland and J. Stake, *IEEE Electron Device Letters,* **33**, 71 (2012).
4. Y.-M. Lin, A. Valdes-Garcia, S.-J. Han, D. B. Farmer, I. Meric, Y. Sun, Y. Wu, C. Dimitrakopoulos, A. Grill, P. Avouris and K. A. Jenkins, *Science,* **332**, 1294 (2011).
5. H. Madan, M. J. Hollander, M. LaBella, R. Cavalero, D. Snyder, J. A. Robinson, and S. Datta, in *Proc. Int. Electron Devices Meeting*, (2012).
6. J.A. Robinson, M. Wetherington, J.L. Tedesco, P.M. Campbell, X. Weng, J. Stitt, M. Fanton, E. Frantz, D. Snyder, B.L. VanMil, G.G. Jernigan, R.L. Meyers-Ward, C.R. Eddy, D.K. Gaskill, *Nano Lett.*, **9**, 2873 (2009).
7. J. Röhrl, M. Hundhausen, K. V. Emtsev, T. Seyller, R. Graupner, L. Ley, *Appl. Phys. Lett.,* **92**, 201918 (2008).
8. D. Graf, F. Molitor, K. Ensslin, C. Stampfer, A. Jungen, C. Hierold, L. Wirtz, *Nano Lett.*, **7**, 238 (2007).
9. J. A. Robinson, M. Hollander, M. LaBella, K. A. Trumbull, R. Cavalero, and D. W. Snyder, *Nano Letters* **11** (9), 3875 (2011).
10. M. Hollander, A. Agrawal, M. Bresnehan, M. LaBella, K. Trumbull, R. Cavalero, D. Snyder, S. Datta, and J. Robinson, *Phys. Solidi Status*, (under review), (2013)
11. F. Speck, J. Jobst, F. Fromm, M. Ostler, D. Waldmann, M. Hundhausen, H. B. Weber, and Th. Seyller, *Appl. Phys. Lett.*, **99**, 122106 (2011).
12. J. A. Robinson, M. LaBella, M. Zhu, M. Hollander, R. Kasarda, Z. Hughes, K. Trumbull, R. Cavalero and D. Snyder, *Applied Physics Letters,* **98**, 053103 (2011).
13. M. J. Hollander, M. LaBella, Z. R. Hughes, M. Zhu, K. A. Trumbull, R. Cavalero, D. W. Snyder, X. Wang, E. Hwang, S. Datta and J. A. Robinson, *Nano Letters,* **11**, 3601 (2011).